Construction and Building Materials 239 (2020) 117867

Contents lists available at ScienceDirect

Construction and Building Materials

journal homepage: www.elsevier.com/locate/conbuildmat

Permeability and elastic properties assessment of alumina nanofiber (ANF) cementitious composites under simulated wellbore cyclic pressure

Phillip D. McElroy *, Hossein Emadi, Daniel Unruh

Texas Tech University, Lubbock, TX, United States

HIGHLIGHTS

- Alumina nanofibers (ANF's) dispersion assessed by transmission electron microscope.
- Cement cured at 82.2°C with 20.68 MPa for 24 hours to emulate wellbore conditions.
- Alterations in permeability, compressive strength, and elastic properties assessed.
- Microstructural assessments using X-Ray Diffraction and Thermogravimetric analysis.

ARTICLE INFO

Article history:
Received 31 July 2019
Received in revised form 10 December 2019
Accepted 12 December 2019

Keywords:
Alumina nanofiber (ANF)
Elastic properties
Degree of hydration (DOH)
Chemically bound water (CBW)

ABSTRACT

Highly dispersed Alumina Nanofibers (ANF's) were utilized in oil well cement class "H" to investigate effects of ANF's on the cement's mechanical and microstructural properties under simulated wellbore conditions. Cement composites consisted of a reference (Ref) sample containing no ANF's and three additional formulations with 0.1%, 0.2%, and 0.3% ANF's by weight of cement (BWOC) incorporated in cement formulations with various common additives. The provided producing liquid dispersion methodology was assessed using a Transmission Electron Microscope (TEM) with each composite formulation undergoing permeability and elastic property testing under simulated cyclic confining wellbore pressures. The compressive strength was also measured along with a microstructural assessment. The microstructural assessment consisted of measuring the formation of hydration products using an X-ray diffractogram (XRD) and thermogravimetric analyzer (TGA). The results indicate that 0.1% of ANF provides the greatest increase in mechanical properties and possesses the lowest permeability through all pressure cycles. Additionally, the amount of Calcium Silicate Hydrate (C-S-H) and Degree of Hydration (DOH) was maximized for 0.1% ANF compared to other composite formulations.

Published by Elsevier Ltd.

1. Introduction

The oil well cementing operation involves placing cement slurry several thousands of feet below the surface of the earth in order to provide structural support for the casing and wellbore. The cement sheath is also designed to provide complete zonal isolation, preventing uncontrolled flow of reservoir fluids. Cement sheath failure can severely impede the ability of the well to produce efficiently leading to lost revenue from production, hazardous rig and producing operations, and deleterious environmental issues [1]. Beginning from the drilling phase, to the plug and abandonment (P&A) phase, the cement sheath is constantly exposed to various thermal and cyclic mechanical loading. In-situ conditions of various stresses, elevated temperatures, and pressures are the primary cause of weakening and failure of the cement sheath [2,1]. The fluctuating conditions can also potentially cause cracks and micro-annuli. This is particularly problematic in cement sheaths, allowing a pathway for gas to migrate to surface [3]. A study examining the number of wells reported worldwide (Australia, Austria, Bahrain, Brazil, Canada, the Netherlands, Poland, the UK and the USA) indicate that up to 75% of wells have had some form of well barrier or integrity failure [4].

The search for alternative materials to improve mechanical performance, in the oil well cementing operation, has continued for decades [5]. Currently, nanotechnology is continually being implemented to improve the oil well cementing process. Utilization of

* Corresponding author.
E-mail addresses: phillip.mcelroy@ttu.edu, mac.phillip@gmail.com (P.D. McElroy).

https://doi.org/10.1016/j.conbuildmat.2019.117867
0950-0618/Published by Elsevier Ltd.

nanomaterials in oil well cements is a promising methodology to alter conventional cement systems into multifunctional, durable composites capable of withstanding stressful conditions for the entire life of the well [6]. Cement failure initiates from the nanoscale where macrofibers and microfibers are not effective [7]. Among composite nanoscale reinforcement material, graphene ring-based materials have received majority of research efforts [8]. Most notably, carbon nanotubes (CNTs) and nanofibers (CNFs) have attracted substantial attention due to their extraordinary strength properties in terms of tensile strength (Giga Pascal (GPa)) and modulus of elasticity (Tetra Pascal (TPa)) [9–13]. However due to the high hydrophobicity and the tendency of graphene material to agglomerate, owing to Van der Waals forces, obtaining an adequate dispersion is an arduous task and the cost of such material is substantially high [5,14]. Nanofiber agglomeration infamously diminishes the mechanical properties of fiber-reinforced composite materials [15]. This can be catastrophic in wellbores considering the cement sheath, between the formation and casing, is subjected to various loads [16]. Goodwin and Crook concluded cement sheaths with high compressive strength provided better casing support but lacked zonal isolation capabilities with excessive internal casing pressure [17]. They also concluded cement sheaths with a higher Young's Modulus (MOE) undergoing pressure and temperature fluctuations, are more susceptible to damage than cement sheaths with a lower MOE [17]. Zhaoguang Yuan examined cyclic confining pressure of class "G" cement and concluded a higher Poisson's ratio exhibits better cycle fatigue behavior [18]. Although, examination of one parameter (compressive strength, MOE, Poisson's ratio, etc.) is insufficient information in order to characterize a cement system subjected to cyclic loading and unloading [19]. Despite recent technological advancement in smart polymeric materials, fibers and self-healing materials, it is still a big challenge to provide adequate long-term zonal isolation in severe oil well conditions [6]. Nanomaterials considered nascent, when utilized to improve long-term zonal isolation, have therefore continually increased in concerted research efforts. For example, cellulose nanocrystal (CNC) were combined with Type G oil well cement to favorably transform the internal air-void network while increasing the compressive and tensile strength of the cementitious formulation [20].

γ-alumina nanofibers (ANF's) is a relatively new type of reinforcement nanomaterial functionalized by aluminum, zirconium, nickel, and copper oxides [21]. ANF's have drawn noteworthy attention, in various industries, as a low cost 1D nanofiber possessing high strength, stability at 1200 °C, low thermal conductivity, and corrosion resistance. Beyond 1200 °C the γ structure changes drastically resulting in the formation of the α phase. ANF's have aspect ratios (length-to-diameter ratio) of 18–120:1, allowing effective bonding with various hydration products in cement [22]. Utilizing γ-alumina nanofibers rather than traditional particulate γ-alumina is of great cement technological application [21]. Despite the potential upside, research of ANF's in oil well cement has not been thoroughly investigated.

The present work first focused on assessing the quality of ANF's dispersed in deionized water. Next, the permeability of the cementitious composites was studied under cyclic confining pressure. The solution was also incorporated in the cement mixture at various ANF concentrations and compressive strength tests were performed. Additionally, the two mostly commonly referenced elastic properties [23] MOE and Poisson's Ratio were also measured dynamically under the same cyclic confining pressure schedule. The microstructural analysis (physical or chemical interaction) between the ANF's and the cement paste were also examined and discussed. Lastly, a brief discussion on the operational costs were discussed based upon conditions in the Permian Basin.

2. Experimental program

2.1. Raw materials

Aluminum oxide (γ-Al_2O_3) nanofibers synthesized by oxidizing aluminum in controlled liquid phase, were purchased from ANF technology (Europe). Highly bundled ANF's were purchased, as well as a 2% pre-dispersed solution. The physical properties of ANF's are shown in Table 1.

Class "H" oil well cement, which is used by nearly 80% of oil drilling companies [5,24], was used as the binder material. The chemical composition consists of 52% C_3S, 25% C_2S, 12% C_4AF, 5% C_3A, and 3.3% $CaSO_4$. Bentonite, a colloidal clay mineral primarily composed of the mineral (smectite) $NaAl_2(AlSi_3O_{10})(OH)_2$, was used as an extender. Bentonite is the most commonly used additive to lower cement slurry density [25–27]. CFR-3 (Cement friction reducing) agent, which is a sulfonic acid salt, with a specific gravity of 1.17, bulk density of 0.61 g/cm^3, and ph of 7–9 was used as a dispersant.

2.2. Pre-dispersion assessment

The 2% pre-dispersed ANF solution was prepared by using a disintegrator to break the fibers into smaller particles representative of Table 1. The fibers are then incorporated into deionized water according to the target percentage loading. The mixture is placed in a dispersion container where the maximum ultrasonic sonotrode strength is 1000 W. It should be mentioned the exact methodology of producing the 2% pre-dispersed solution is absent due to the company's trademark restriction.

In order to assess the efficacy of the 2% pre-dispersed solution, the same sample concentration was prepared differently to observe differentiations. A ball milling device (8000 M Mixer/Mill) set to pulverize samples at 1080 cycles per minute, was used to grind 1 g of ANF bundles into the appropriate size range (Table 1) for a total of 25 min. The fibers are then placed in a dispersion container containing 50 g of deionized water. The container is placed in an ultrasonication bath (Cole-Parmer 8891) with an energy delivery set at 210 W for 10 min. A built-in temperature sensor prevents overheating, automatically halting the ultrasonication process for a brief period.

For testing, both samples are diluted with deionized water by a factor of 25 and each sample is sonicated for 10 min before observations. The diluted samples are drop cast onto carbon coated copper grids to dry. Transmission electron microscope (TEM) images are taken by Hitachi H8100 at an accelerating voltage of 200 kV. Two samples were prepared to observe the pre-dispersed solution's efficacy and to determine if there is any noticeable difference between the dispersibility of ANF's in aqueous solutions with varying dispersive methodologies.

2.3. Cementitious composite preparation

50.8 mm cube specimens were utilized for compressive testing while cylindrical specimens had a size of 38.1 mm diameter × 50.8 mm length for testing dynamic elastic properties and permeability under stepwise loading and unloading schedules. All cement slurry specimens were prepared with a water-to-cement ratio of 0.55. The dosage of ANF's varied for each mixture, (Table 2) displays the experimental cement compositions.

Plain cement batches, without any ANF's, were cast as a reference. Three different batches of varying ANF concentrations consisting of 0.10%, 0.20%, and 0.30% by weight of cement were also prepared. Four replicates were prepared for each batch of cement

Table 1
Properties of ANF's.

Type	OD	Length	Purity	SA	pH	TS	Density
γ-Al_2O_3-OH	2.7–10 nm	100–900 nm	99.9%	150–160 m^2/g	6.4–6.8	1100 °C	3.89 g/cm^3

Note: OD-Outer Diameter; SA-Surface area; ph-Potential of Hydrogen; TS-Thermal Stability.

Table 2
ANF reinforced cementitious composite compositions.

Composite Identifier	Cement (g)	Water (g)	ANF (g)	CFR-3 (g)	Bentonite (g)	ANF/cement wt%
Ref	800	440	0	1.50	20.0	0
ANF-1	800	440	0.80	1.50	20.0	0.10
ANF-2	800	440	1.60	1.50	20.0	0.20
ANF-3	800	440	2.40	1.50	20.0	0.30

and the experiment was conducted at least twice for repeatability purposes.

Mix water was placed in the constant speed blender and blended at a constant rotational speed of 419 rad/s for 15 s. The dry blended solids were uniformly added to the water during the 15 s duration, afterwards the rotational speed is automatically increased to 1257 rad/s for an additional 35 s. The mixture was then poured into four previously thinly greased 50.8 mm cube molds, at approximately one-half of the mold's depth. Each specimen was puddled 25 times and stirred to eliminate segregation and dislodge any air bubbles. The remaining one-half of the mold was filled and the puddling operation was repeated. The specimens were placed in a high temperature high pressure (HTHP) curing chamber, to emulate wellbore conditions, and demolded after curing at 82.2 °C with 20.68 MPa for 24 h. All procedures were done in accordance with API 10B-2 [28].

Conversely, after specimens were demolded 38.1 mm diameter cement cores were sub sectioned using a Wilton variable speed drill press with a 38.1 mm diamond-tipped core drill bit producing cylindrical specimens. Specimens were then placed in a vacuum oven at 100 °C until there was ≤0.1% weight variation over 24 h, a commonly used technique [29–31].

2.4. Cementitious composite characterization tests

2.4.1. Permeability measurements

NER AutoLab 1500 (New England Research, Inc., White River Junction, VT, USA) (Fig. 1), equipped with a data acquisition system, was used to calculate the permeability of all composite formulations under cyclic confining pressure schedules [32]. After sample jacketing and preparation (Fig. 2), the sample was placed in the high pressure (HP) vessel mounted on a base plug. An electronic console along with three pressure intensifiers were used to accurately control confining pressure.

The confining pressure was initiated at 6.89 MPa using the panel mode on the electronic console. The vent valve was opened with nitrogen, an inert gas, allowing the pore pressure intensifier to be loaded with gas. The permeability specifications were loaded into the data acquisition system and the panel mode was diverted to computer mode, allowing better control of the confining and pore pressures. The pore pressure valve was opened allowing gas to flow in the sample from the upstream side. After the downstream pressure is equal to the upstream pressure (approximately 3.45 MPa) the permeability measurements commenced.

The permeability was measured using the transient step method developed by Brace [33]. During every measurement the confining pressure was maintained at a specified value in order to simulate wellbore conditions. A pressure pulse, Eq. (1) was introduced into the upstream volume and the pressure in the downstream volume, Eq. (2) is recorded. Based upon the downstream pressure pulse the permeability can be derived. Eq. (3) is the partial differential equation that governs pressure changes as a function of distance and time through the composite material. p is the pressure within the sample (MPa),x is the axial distance measured from the upstream face of the sample (m), t is the time (s), Q is the flow rate through the sample (m^3/s), β is the compressibility of the fluid ($N^{-1}\cdot m^2$), V is the downstream volume (m^3), β' is the lumped compressibility ($N^{-1}\cdot m^2$), μ is the pore fluid viscosity (Pa·s), and k is the permeability (Darcy). Only a brief mathematical description of the transient step method is provided. The mathematical details can be found elsewhere [33–36]. Beginning at 6.89 MPa the confining pressure was increased to 20.68 MPa in 3.45 MPa increments and finally decreased in the same manner with the permeability measured at each step. This was done twice, totaling two full pressure cycles.

$$p|_{x=0} = p(t) \tag{1}$$

$$\frac{\partial p}{\partial t} = \frac{Q}{\beta V} \tag{2}$$

$$\frac{\partial^2 p}{\partial x^2} + \beta' \left(\frac{\partial p}{\partial x}\right)^2 = \frac{\beta' \mu}{k} \frac{\partial p}{\partial t} \tag{3}$$

2.4.2. Mechanical properties

Compressive strength (P_c) tests were conducted according to (API-10B) using a uniaxial load frame with a constant load rate of 72 kN per minute. This test is usually done because it often resembles radial stress acting perpendicular to the axis of the wellbore outward toward the formation [37]. A software was used to calculate the compressive strength. Eq. (4) displays the calculation where F (Newton) is the instantaneous maximum force of the specimen at failure, L (m) is the length of the specimen, and W (m) is the width of the specimen.

$$P_c = \frac{F}{L \times W} \tag{4}$$

NER AutoLab 1500 was also used to calculate the dynamic elastic properties MOE (E) and Poisson's Ratio (v) under cyclic confining pressure. An ultrasonic system generated shear pulses (V_s waves) and compressional pulses (V_p waves) propagating through the specimen jacketed in a HTHP rubber sleeve using a source and receiver transducer with wired connections (Fig. 3).

After calculating the bulk density (ρ) (g/cm^3) Eq. (5) where m is the mass (g), r is the radius (cm), and h is the height measured in (cm). The specimen was assembled in the high pressure (HP) vessel mounted on a base plug. The confining pressure was initiated at 6.89 MPa then increased to 20.68 MPa in 3.45 MPa increments

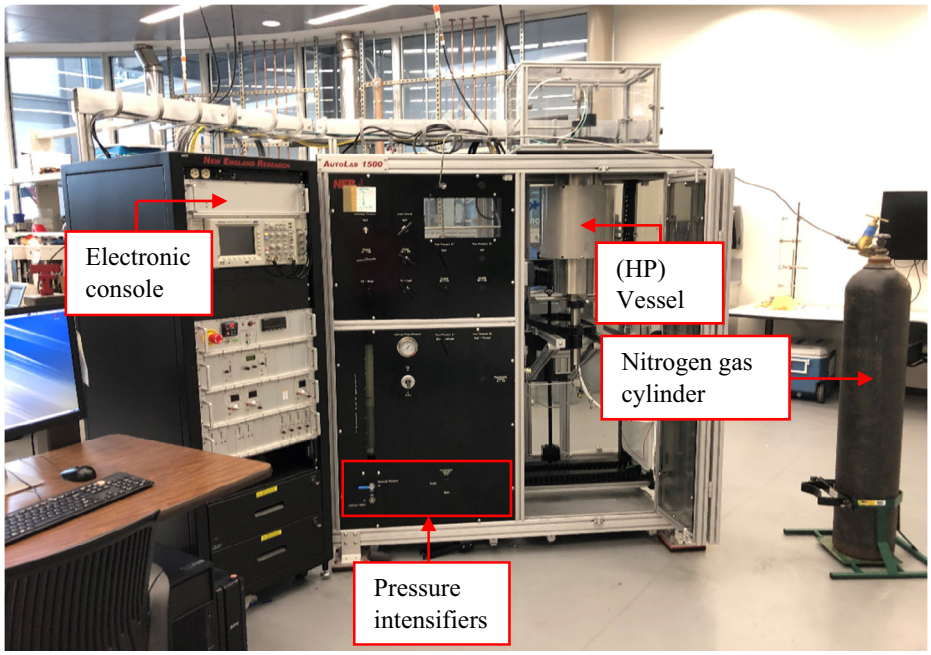

Fig. 1. (NER) AutoLab 1500 system for ultrasonic velocity and permeability measurements.

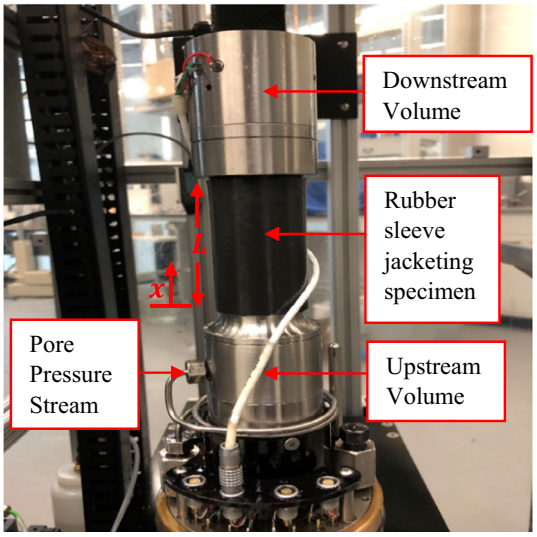

Fig. 2. Assembled sample for permeability measurements.

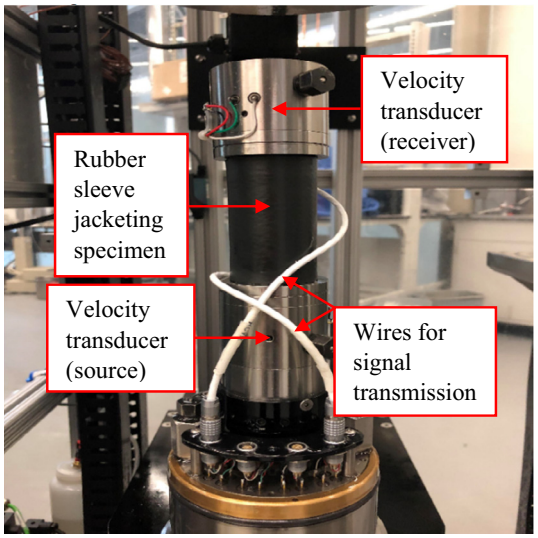

Fig. 3. Assembled cement sample for ultrasonic velocity measurements.

and finally decreased in the same manner for two cycles. Both velocities (V_P and V_s) (m/s) were measured at each confining pressure resulting in the final calculation of MOE Eq. (6) and Poisson's Ratio Eq. (7) [38].

$$\rho = \frac{m}{\pi r^2 h} \tag{5}$$

$$E = \frac{\rho V_S^2\left(3V_P^2 - 4V_S^2\right)}{V_P^2 - V_S^2} \tag{6}$$

$$v = \frac{1 - 2(V_S/V_P)^2}{2\left[1 - (V_S/V_P)^2\right]} \tag{7}$$

2.4.3. Phase transformation evaluation

X-ray diffraction (XRD) analysis was conducted to identify polycrystalline phases of hardened cementitious composites through the recognition of X-ray patterns that are unique to cement crystalline phases [39]. At the conclusion of uniaxial compression tests, cement fragments were taken from the centroid and ground into fine powder (10–20 μm) using a mortar and pestle. Cement hydration was arrested by grounding in an organic solvent (isopropyl alcohol) and rinsing with diethyl ether, afterwards samples were dried in a vacuum oven at 105 °C [40–42]. A powder X-ray diffraction analysis was performed immediately afterwards using a Rigaku Ultima III powder diffractometer in a $\theta - 2\theta$ configuration with CuKα (1.5418 Å) radiation (anode voltage 40 kV and 44 mA). The incident X-ray beam was modified using the Rigaku Cross Beam Optics system to create a parallel beam geometry. Diffraction intensities were recorded on a scintillation detector after being filtered through a Ge monochromator. The patterns were obtained for specimens using a 2θ range of 3–90°. In all instances the data collection rate was set at 3.5 min/° with a step width of 0.02°. The diffraction patterns were analyzed using the software JADE v9.1 in combination with PDF 4+ (2019 version).

2.4.4. Degree of hydration analysis

The thermogravimetric analysis (TGA) was executed using the Mettler Toledo TGA/SDTA851e Module in order to calculate the degree of hydration (DOH). At the conclusion of uniaxial compression tests, cement fragments were taken from the centroid and ground into fine powders with a mortar and pestle while evaporation was minimized. Approximately 30 mg of powder was transferred into the TGA chamber for measurement. The experiment was conducted by placing the specimen in the chamber at ambient temperature then increasing the temperature to 140 °C by 20 °C/min in a purged nitrogen environment. This is the critical temperature for evaporable water as reported in the literature [43]. This temperature was held constant for a total of 25 min to remove evaporable water in the specimen. Afterwards, the specimen was heated from 140 °C to 1100 °C at a rate of 20 °C/min which is necessary to extract all chemically bound water (CBW). The data was normalized with the samples weight at 140 °C taken as the baseline for measurements.

3. Experimental results and discussions

3.1. Morphological characterization of ANF suspensions

When ANF's are introduced to cement paste during the mixing process, a uniform distribution of fibers in the cementitious matrix cannot be expected if they were not previously dispersed well in deionized water. Deagglomeration of nanofibers is essential in obtaining homogeneous dispersions that essentially enhance the mechanical performance of composite materials [44]. Transmission electron microscope (TEM) images, which is one of three common methods used to assess nanomaterial morphology and dispersibility [45], were taken to assess ANF dispersion in water. Fig. 4 displays the ball milled ANF dispersion prepared according to Section 2.2. It is evident there are various zones of nanofiber agglomeration throughout the dispersion, examples are enclosed in hashed red shapes. It is also evident that the ball milling procedure was not effective in producing ANF's in the appropriate size range Table 1 in various areas, examples are enclosed in yellow circles. However, in Fig. 5 the 2% pre-dispersed solution displays the well dispersed solution with ANF's indicative of the size in Table 1. These results indicate the ball milling procedure is chaotic and modifications are necessary to achieve the appropriate size range. Furthermore, without proper sonication ANF's can easily agglomerate, meaning the ultrasonication process should also be modified. Yonathan Reches [46] also experienced suspended γ-Al_2O_3 nanoparticle agglomeration without proper sonication. These results affirm the notation that without proper preparation and ultrasonication methods, nanofibers with large aspect ratios and Van der Waals forces cause significant agglomeration [47]. Essentially the 2% pre-dispersed solution displayed an exceptional dispersibility and was used for the remainder of the cement experiments.

3.2. Permeability measurements

Figs. 6–9 displays the permeability measurements during cyclic loading and unloading at each confining pressure value for all cement formulations. The experiments were performed under cyclic confining pressure beginning at 6.89 MPa, increased to 20.68 MPa in 3.45 MPa increments, and finally decreased in the same manner for two cycles. All cement formulations undertake the most irreversible change to the pore structure during the first pressure cycle. This irreversible change indicates the closing of microcracks due to increasing the confining pressure. All cement formulations also showed the ability to endure confining pressure fluctuations since there was no sudden increase in permeability which would indicate internal cement failure. Although subtle, there are minor changes in permeability between cement formulations. The Ref cement sample had an average permeability of 1.83 micro Darcy (μD), ANF-1 had an average permeability of 1.44 μD, ANF-2 had an average permeability of 1.92 μD, and ANF-3 had an average permeability of 2.25 μD. The increase of permeability between the Ref cement paste and the ANF-1 cement paste is due to the characteristics of ANF's. ANF's possess high aqueous

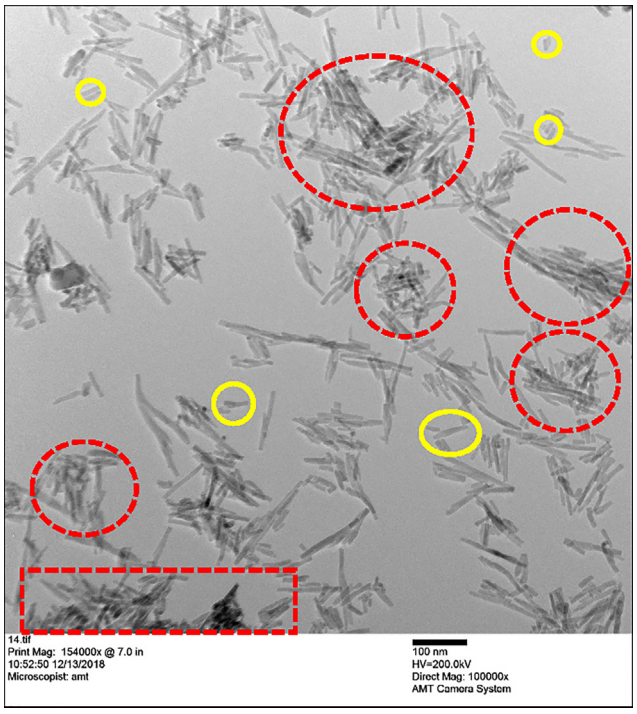

Fig. 4. Ball milled dispersion solution.

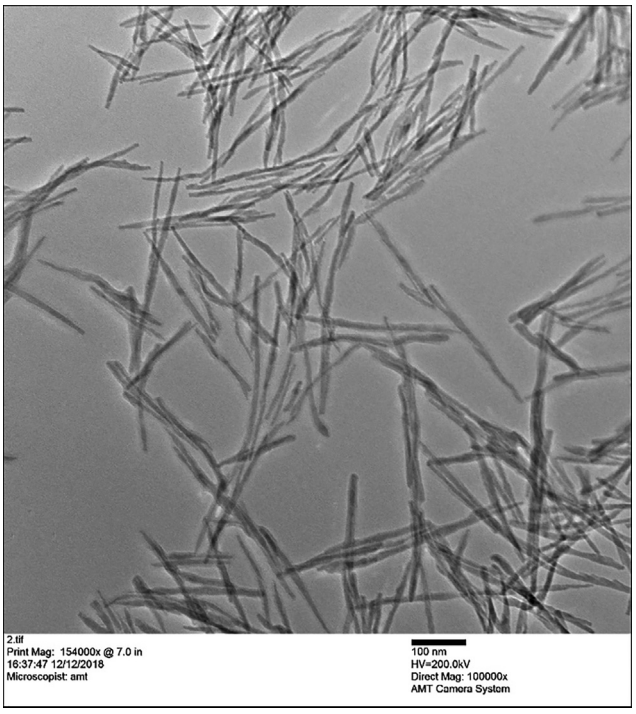

Fig. 5. 2% pre-dispersed solution.

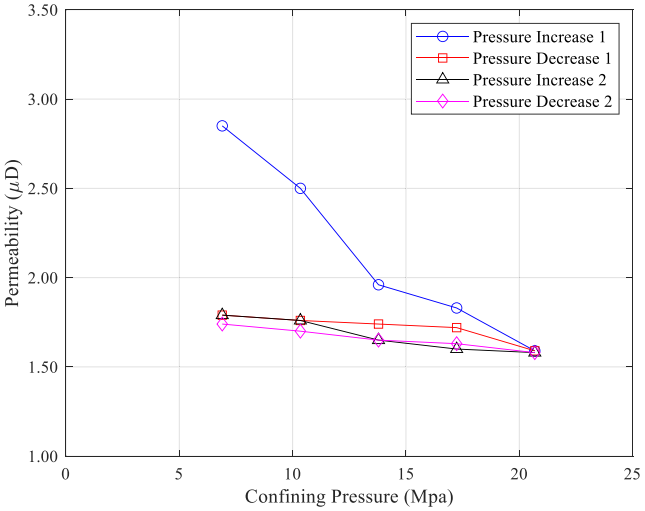

Fig. 6. Permeability measurement of Ref cement composite under cyclic confining pressure.

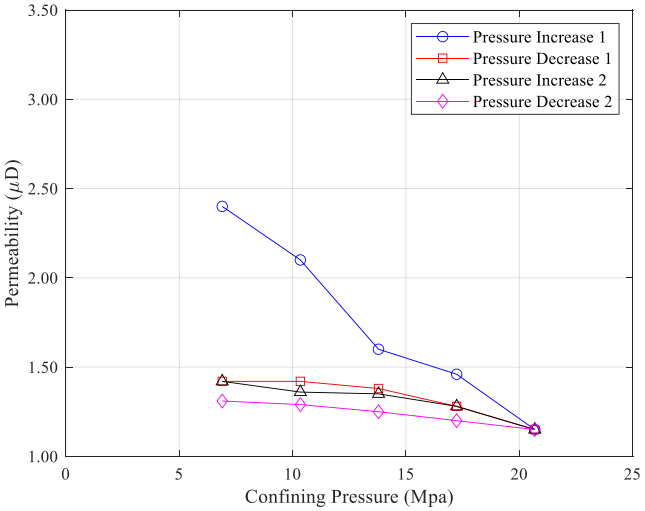

Fig. 7. Permeability measurement of ANF-1 cement composite under cyclic confining pressure.

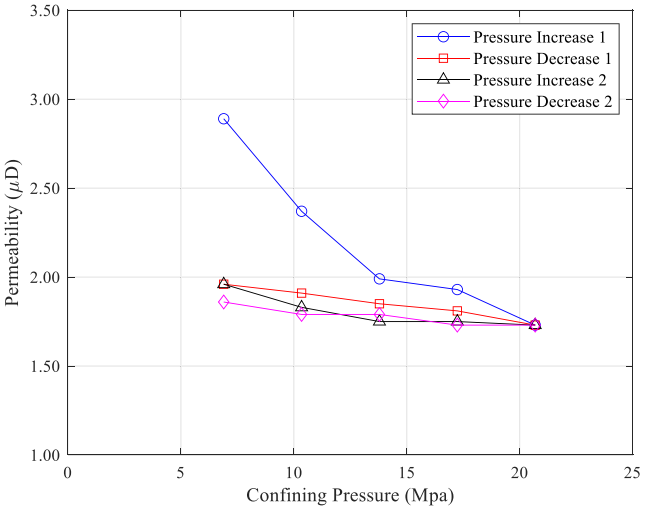

Fig. 8. Permeability measurement of ANF-2 cement composite under cyclic confining pressure.

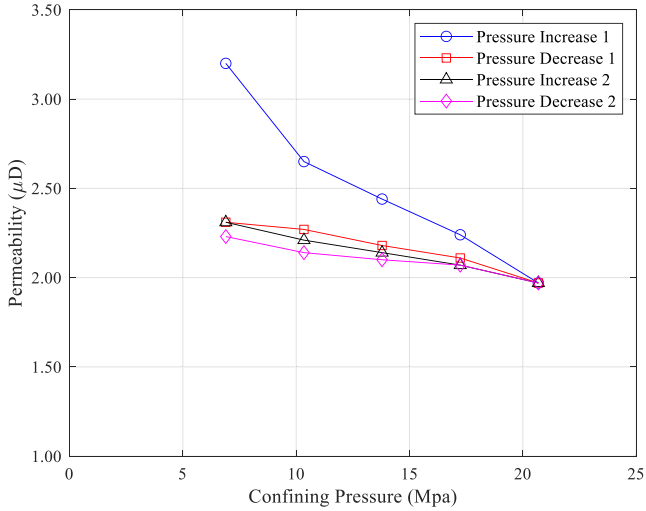

Fig. 9. Permeability measurement of ANF-3 cement composite under cyclic confining pressure.

adsorption capacity. This allows cement particles to hydrate around ANF's, which creates a denser microstructure filling nano-pores and bridging nano-cracks. ANF's essentially provide nuclei for cement phases to promote degree of hydration (DOH). The inclusion of ANF's also increases the amount of calcium silicate hydrate (C-S-H) within the cement composite, this will be further discussed in the XRD analysis section. Thus, the amount of binder is increased which reduces the permeability of the cement and densifies the structure. However, after ANF-1 the permeability of composites steadily increases with the increase of ANF's. This increase of permeability is due to nanofilament agglomeration and clustering due to increased loading. This leads to irregularities in the microstructure during the hydration process which increases the permeability. These irregularities in the microstructure can easily cause nano or microcracks in the composite which can be enhanced by the simulated downhole curing temperature. Mahmoud [48] experienced a similar phenomenon stating that after increasing the nanoclay content past 3%, the permeability of cement increased.

3.3. Mechanical properties

3.3.1. Compressive strength

Fig. 10 illustrates the variation of compressive strength values with formulations presented in Table 2 after curing at 82.2 °C with 20.68 MPa for 24 h. According to the graph it is evident that composition ANF-1, containing 0.1% ANF by weight of cement (BWOC), possesses superior strength gain at 25.6 MPa compared to the Ref composite at 17.8 MPa. This estimates to a 44% increase in uniaxial compressive strength. This dramatic increase is crucial considering the fleeting wait on cement (WOC) time. The strength gain from all the experimental composites is primarily a result of the hydration products at elevated temperatures. Hydration is a function of temperature which affects the kinetics and mechanisms of hydration. Cement slurries cured at temperatures above ambient conditions result in a hydration acceleration effect leading to a higher hydration degree and subsequently, producing a more condensed composite with higher compressive strength. The difference is ANF's act as a nucleation site in cement composites, with hydration products (mainly calcium silicate hydrate (C-S-H)) forming around the nanofibers providing nano-reinforcement [49]. Essentially when nanocracks begin to form at the C-S-H level, ANF's can impede their progression due to the "bridging effect" in the elastic region.

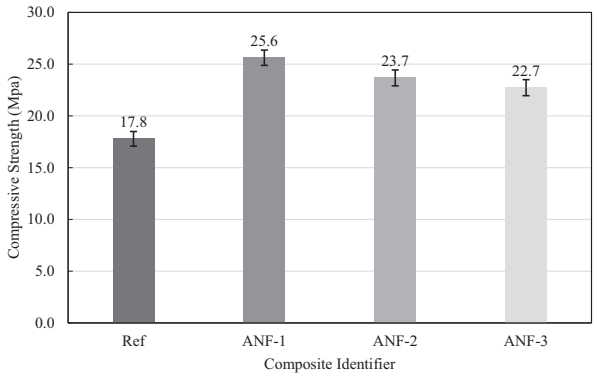

Fig. 10. Compressive strength of specimens.

Fig. 10 also illustrates a decrease in strength gain, compared to ANF-1, with composites ANF-2 and ANF-3 at 23.7 MPa and 22.7 MPa respectively. This strength decrease is due to nanofiber clustering with higher dosages of nanomaterial [50]. This result affirms the belief that at high loading of nanofibers, there is difficulty in dispersing the material uniformly throughout the composite material due to Van der Waals forces.

3.3.2. Elastic properties

The dynamic elastic properties, MOE and Poisson's ratio, were also measured under the same cyclic confining pressure schedule as the permeability tests. The MOE data is shown in Fig. 11. According to the results, it is evident all cement formulations either experienced insignificant or no change in MOE. Specimens are experiencing a low inelastic deformation (the closing of microcracks), as the MOE values are mostly able to return to its original value after pressure cycling. These values are similar to Spaulding [51], who reported MOE values of class "H" cement between 5.5 GPa to 11.1 GPa with varying cement class "H" formulations. The Ref cement composite displays the highest elastic modulus, which does not contain any ANF while the ANF-1 displays the lowest elastic modulus from all other cement formulations. It is interesting to note that ANF-2 and ANF-3 display similar values as the Ref material. A possible explanation is that the cements are experiencing nanofiber clustering which reduce the mechanical properties, thereby lowering elasticity. This is essential because cements with lower MOE are more resistant to common mechanical stresses associated in well operations [52].

It is also worth noting that as confining pressure increases, the V_p and V_s waves also increase. Essentially the confining pressure is causing microfractures to close, thereby increasing the velocity which causes the specimens to exhibit plastic behavior. This explains the increase of MOE for each cement composition. In order to effectively illustrate this phenomenon all MOE values at the corresponding pressure increment were averaged and plotted (Fig. 12). The values were averaged because the YM at the corresponding pressure increment differed minimally across cycles. The standard deviations (SD_x) along with the percentage increase between each averaged pressure increment is also displayed in Fig. 12.

According to Fig. 12, the change in MOE across all pressure fluctuations is the lowest for the ANF-1 sample at 1.23%. Followed by the Ref sample at 1.43%, ANF-2 at 2.93%, and ANF-3 at 3.27%. This is indication that there is more pore volume in the Ref, ANF-2, and ANF-3 cement formulations than the ANF-1 formulation. These results coincide with the permeability results discussed earlier. The ANF-1 sample essentially contains the least amount of pore spaces with an almost constant YM throughout pressure cycling.

Fig. 13 displays the Poisson's ratio values under the same cyclic loading schedule. At each confining pressure increment ANF-1 possesses the highest Poisson's ratio compared to the other cement formulations. Again, the Ref material does not contain ANF which explains the low Poisson's ratio. ANF-2 and ANF-3 however possess slightly lower values of Poisson's ratio than ANF-1. This is possibly due to nanofiber clustering, which lowers the mechanical properties. It is advantageous to increase the Poisson's ratio because this reduces the compressibility of the cement allowing better wellbore integrity. Again, the Poisson's ratio values differed minimally across corresponding pressure cycles, so the values were averaged. The standard deviations (SD_x) along with the percentage change for each averaged pressure increment is also displayed in Fig. 14. Unlike MOE, Poisson's ratio does not display any significant trend as the values slightly increase and decrease between pressure fluctuations. Therefore, it is observed the Poisson's ratio is mostly unaffected by the pressure fluctuations.

3.4. Microstructural analysis

3.4.1. XRD analysis

In order to investigate the phase identification and crystalline phase changes of cement composites cured with ANF's, XRD analysis was conducted with varying dosages of ANF's. Fig. 15 displays

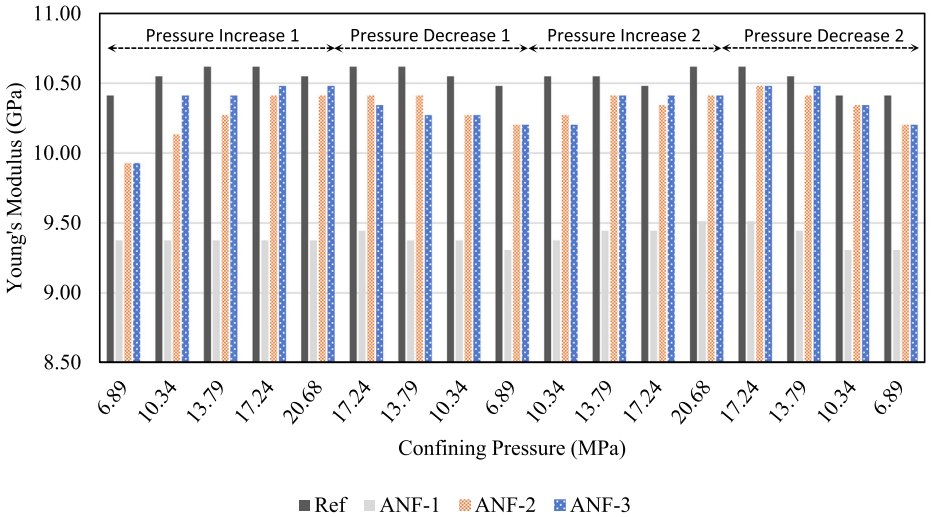

Fig. 11. YM results for each cement composite at the corresponding confining pressure increment for both pressure cycles.

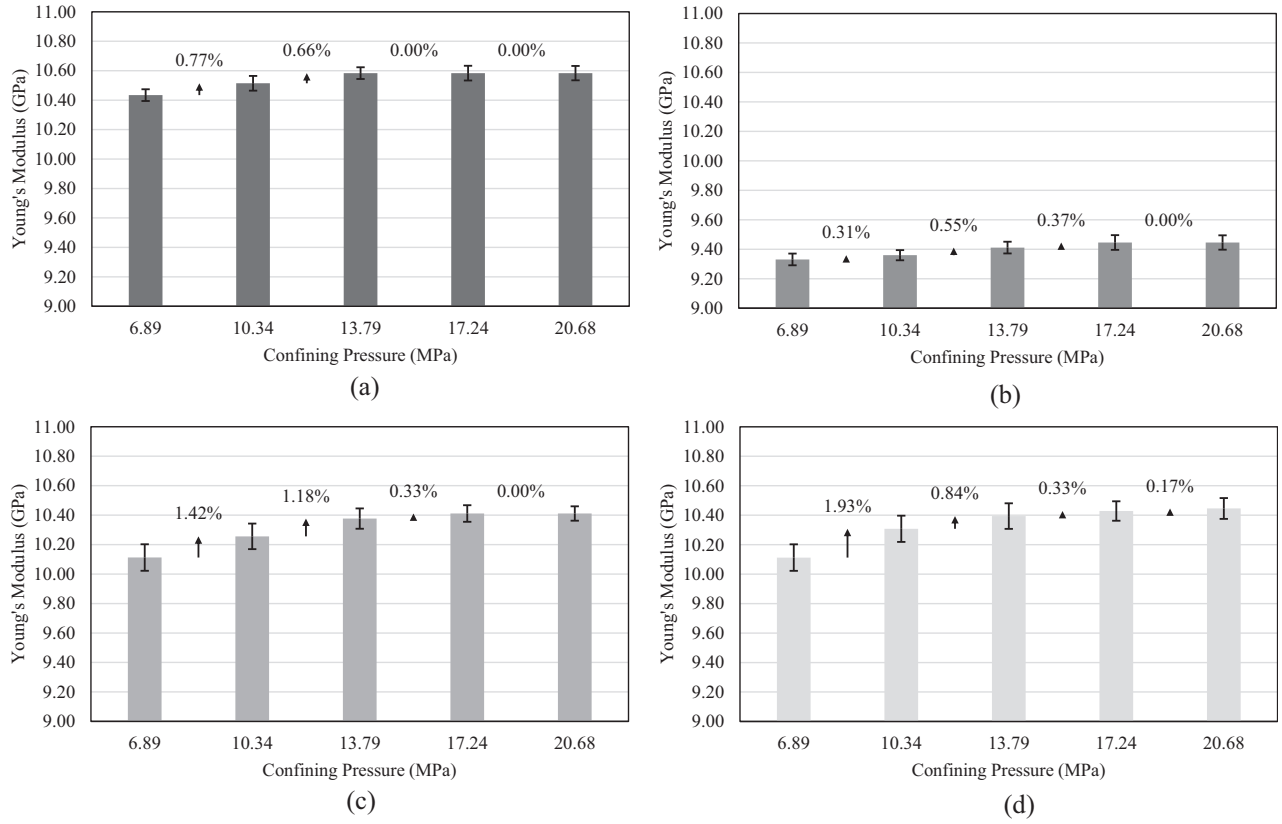

Fig. 12. Average values of Young's Modulus, the percentage increase, and standard deviations of cement composites under cyclic pressure increments. (a) Ref sample (b) ANF-1 (c) ANF-2 (d) ANF-3.

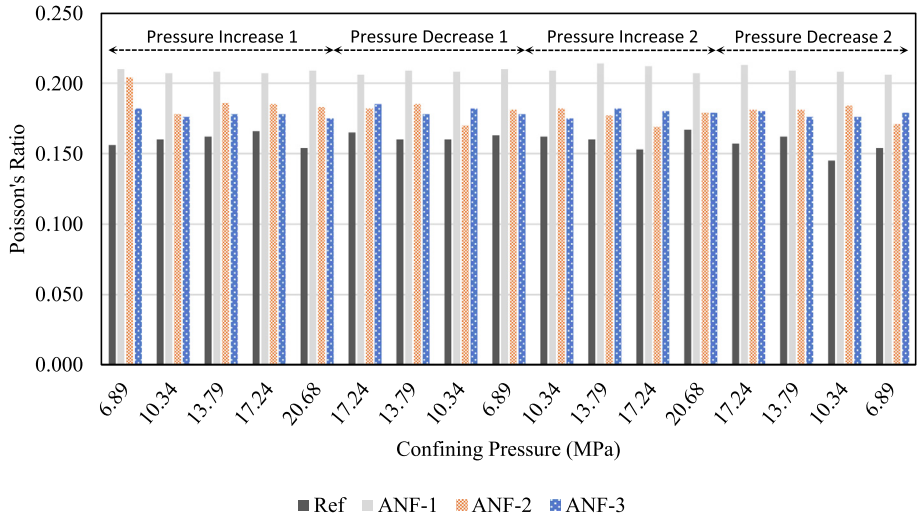

Fig. 13. PR results for each cement composite at the corresponding confining pressure increment for both pressure cycles.

the diffraction patterns of hydrated cement composites listed in Table 2. The XRD patterns reveal that all cement composite formulations experience the same diffraction patterns and trends. Although, there are slightly noticeable differences in the peak intensities. The anhydrous hydration products (Brownmillerite (Ca_2FeAlO_5), Portlandite ($Ca(OH)_2$), Quartz (SiO_2), Calcite ($CaCO_3$), and Larnite ($Ca_2(SiO_4)$)) are crystalline, therefore their detection by X-ray diffraction (XRD) was possible. However, majority of the hydration products was indistinguishable by XRD due to the ill-defined hydrated calcium silicate hydrate gel. This phase is usually referred to as C-S-H which is partially crystalline or amorphous and is structurally related to tobermorite and jennite (with approximate stoichiometry of $C_5S_6H_5$ and $C_9S_6H_{11}$ respectively). Due to the peak overlapping, it is difficult to conduct a quantitative analysis based upon the peak intensities. However, the weight percentage of hydration products for each cement composite was obtained (Table 3). Table 3 was calculated using the semi-quantitative analysis through Rietveld refinements.

Most notable in Table 3 is the amount of C-S-H in each cement formulation. The C-S-H phase is the most vital phase due to its

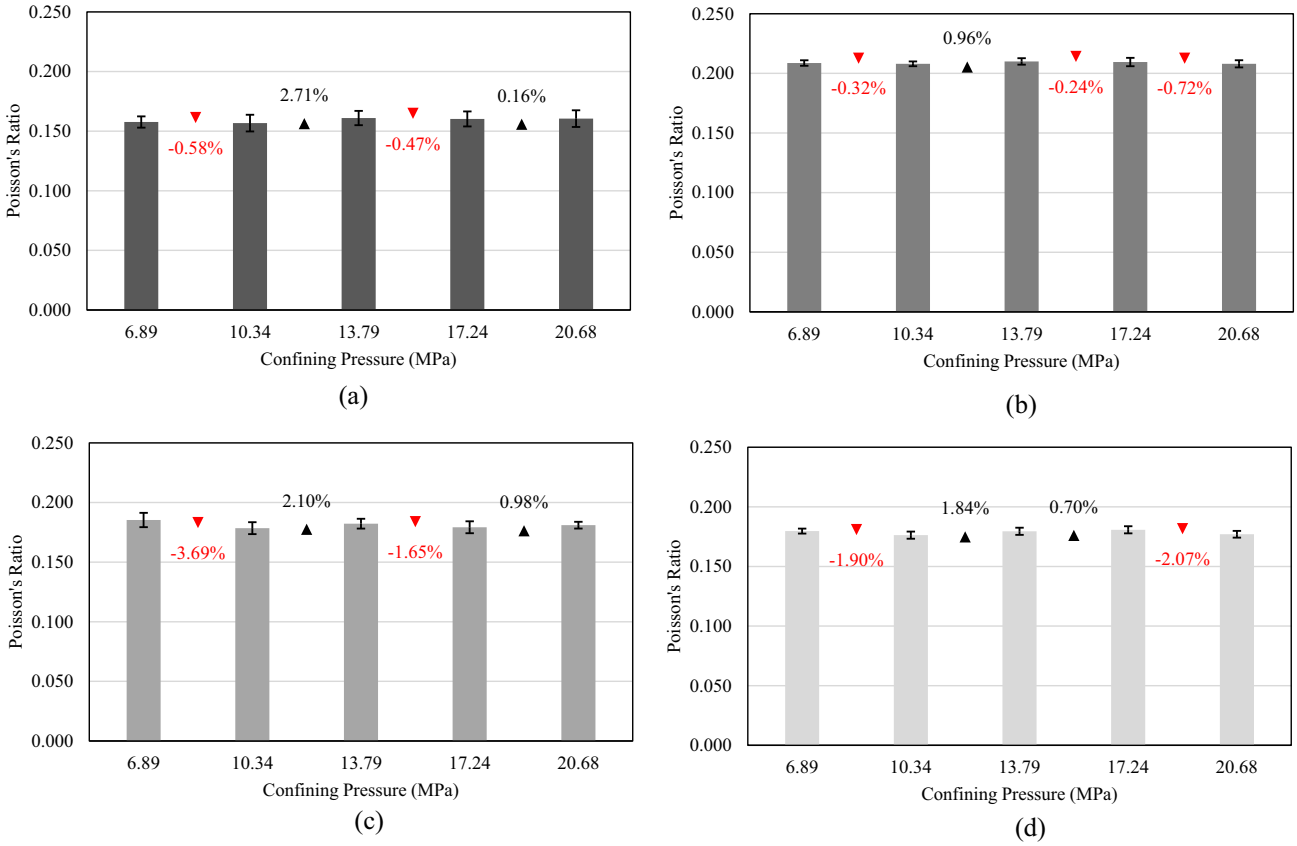

Fig. 14. Average values of Poisson's ratio, the percentage change, and standard deviations of cement composites under corresponding cyclic pressure increments: (a) Ref sample (b) ANF-1 (c) ANF-2 (d) ANF-3.

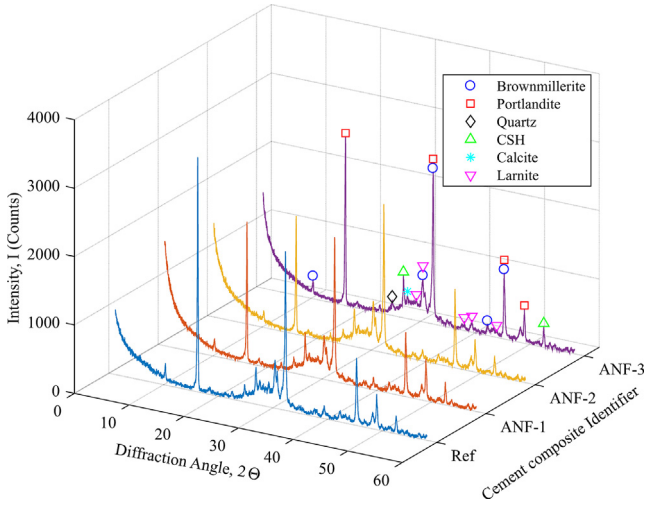

Fig. 15. Diffraction patterns of ANF-cement composites.

binding ability which is responsible for majority of strength gain in hydrated cement specimens. According to Table 3 the largest increase in the C-S-H phase occurred between the Ref and ANF-1 sample. Additionally, the total weight percentage of hydration products ANF-2 and ANF-3 slightly varied from ANF-1. There are two different phenomena that could explain the increase in the C-S-H phase from the Ref sample to the other ANF composite formulations. (1) There is a nucleation effect of ANF's in the cement composite which accelerate the formation of hydrate phases. In other words, there is a seeding effect that is commonly associated with the use of nanomaterials that effectively accelerates hydration. Essentially the seeding effect provides additional surface area which offers more nucleation sites for C-S-H formation. Muzenski [53] utilized ANF's in ultra-high strength cement-based composites in which ANF's were found to act as seeds to promote the formation of hydration products along the fibers. It was concluded that C-S-H formed around nanofibers establishing a "shish kebab" effect. According to the results in this research, the seeding affect phenomena is likely affirmed. (2) The additional presence of Al_2O_3 may also promote the formation of tobermorite. Meller

Table 3
Weight percentage of hydration products in cement composites.

Cement Identifier	Portlandite	Quartz	Calcite	Brownmillerite	Larnite	C-S-H
Ref	32.8	2.4	1.9	10.3	16.6	35.9
ANF-1	29.7	3.3	0.8	11.2	16.3	38.7
ANF-2	28.9	3.1	0.9	11.5	17.9	37.7
ANF-3	29.7	4.2	0.9	10.4	16.7	38.0

[54] conducted experiments on API Class "G" oil well cements were the addition of alumina promoted the formation of tobermorite, thereby, improving the engineering properties of the cementitious composite material. The Al^{3+} ions support the anomalous 1.1 nm tobermorite at high curing conditions which encourages its formation. Likewise, a similar phenomenon is possibly occurring with the addition of ANF promoting the increase of C-S-H owing to the Al^{3+} ions. Since there is such a small additional amount of ANF introduced in the cement composite all the hydration products had a relatively small difference between ANF-1, ANF-2, and ANF-3.

It is also worth noting in situations where sulfate resistance is required, the quantities of tricalcium aluminate are typically reduced or almost eliminated due to its susceptibility of sulfate attack. According to the Ref. sample of Fig. 15, the exclusion of ettringite from the diffraction pattern ascribes to low amounts of tricalcium aluminate. Thus, it seems reasonable that the inclusion of ANF could be deleterious to the cement sheath. However, once ANF is included in the cement composition for samples ANF-1, ANF-2, and ANF-3, there is almost no change in the diffraction pattern. Therefore, the results suggest a low dosage of ANF does not conduce sulfate attacks. Additionally, ANF are considered to be anti-corrosive materials [50]. Thus, it is observed an insignificant amount of alumina is reintroduced into the cement composition negating the formation of ettringite. Although, longer curing durations or increased ANF dosages may deem different results.

3.4.2. TGA analysis

The degree of hydration (DOH) was calculated by measuring the total mass of chemically bound water (CBW) in each of the cement formulations. Fig. 16 displays the weight loss with the mass at 140 °C normalized at 100%. There is also a zoomed in plot of the figure to provide greater details of the weight losses. The dramatic increase in weight loss between 440 °C and 520 °C is attributed to the decomposition of Portlandite ($Ca(OH)_2$) [43] for all samples.

The weight of (CBW) is quantified in Table 4 as (w_b), which indicates there is a slight increase in the weight loss for ANF cement composites compared to the reference sample. The total DOH for each cement formulation is also calculated and presented in Table 4. The DOH was calculated by dividing the weight of CBW, in the region between 140 and 1100 °C, by 0.23 which is the assumed gram per unit gram of cement when fully hydrated [55]. It should be mentioned the value of 0.23 is typical for type I Portland cement, although it has also been used in previous studies to calculate the degree of hydration for class "H" oil well cement [56]. Considering its intended use, there is a possibility of slight systematic calculational error. Additionally, because of the various cement phases that act at different rates, the degree of hydration may relate either to individual clinker phases or the entire cement composition rendering a definitive solution problematic. Therefore, the degree of hydration is considered an overall and approximate measurement of the reacted mass fraction of cement irrespective of the phase [57]. The results show that more water reacts with cement when ANF's are present. These experiments, together with XRD, prove the fact that ANF indeed slightly increases the DOH due primarily to the nucleation effect of ANF which accelerates the formation of hydration products.

To illustrate this phenomenon, once cement particles are combined with water, hydration products begin to form in the matrix (Fig. 17). Considering ANF is added and embedded into the cement matrix (Fig. 18), additional hydration products form (seeding effect) and the fibers can bridge nanopores thereby distributing various stresses.

3.5. Construction cost

Depending upon the type of wellbore drilled and cemented, the operational cost will vary. However, in this article, it is considered the well is drilled in the Permian Basin which is the second largest onshore oil field in the world and the largest in the U.S. A typical

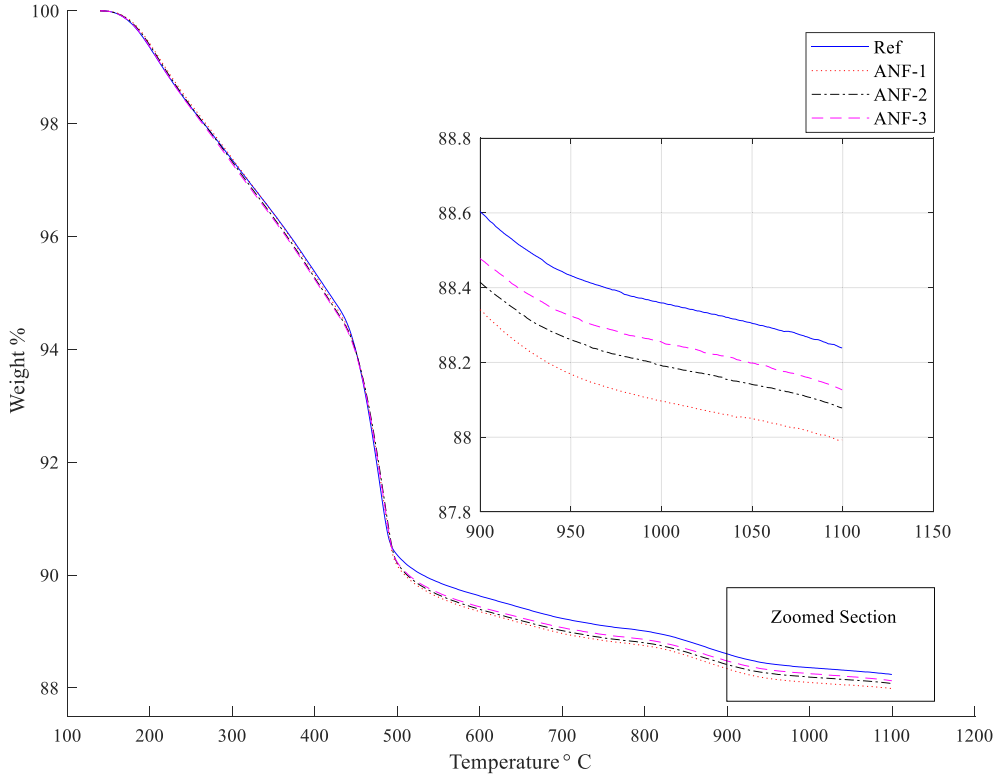

Fig. 16. TGA results from 140 to 1100 °C with the mass at 140 °C as the base (100%).

Table 4
w_b and DOH analyzed per gram of cement paste with different ANF weight fractions.

Analysis	Ref	ANF-1	ANF-2	ANF-3
w_b	11.76	12.01	11.92	11.87
DOH	51.1	52.2	51.8	51.6

w_b: Weight of CBW per g cement; DOH: Degree of Hydration.

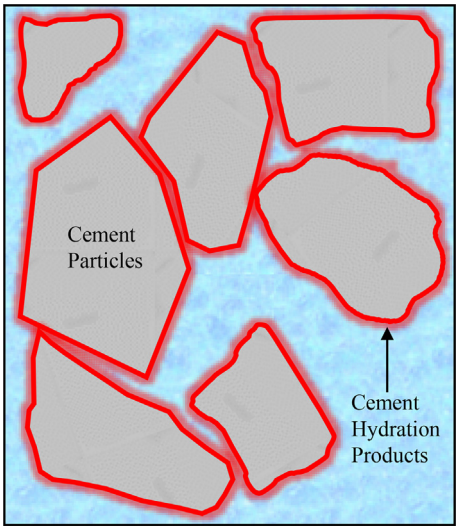

Fig. 17. Schematic representation of cement hydration.

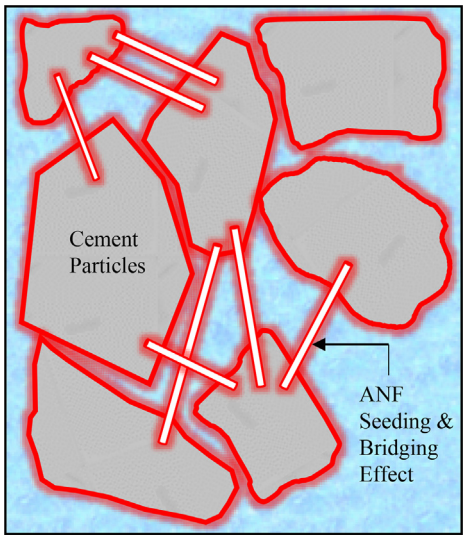

Fig. 18. Schematic representation of cement hydration with ANF.

wellbore trajectory is shown in Fig. 19. Typically, the wellbore is cemented with specialized light weight cement (such as foam cement) until the end of curve (EOC). After the end of curve, the remaining section (lateral section) is cemented with higher density cement. A cross-sectional view of the cemented lateral section is presented in Fig. 20. The cost of ANF is US$1.17/g, which is considerably lower than other nanomaterials such as CNT which can cost upwards of US$750/g. Considering the hole diameter is 215.9 mm and the casing diameter is 177.8 mm, the cost to cement the lateral section with the ANF-1 formulation in Table 2 will cost US$23,780. Considering the improved wellbore integrity ANF can provide, this is a beneficial long-term investment.

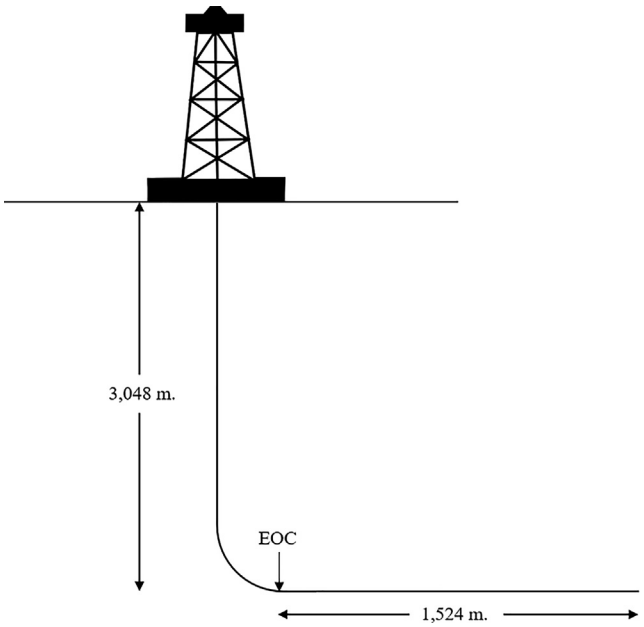

Fig. 19. Schematic of horizontal wellbore trajectory.

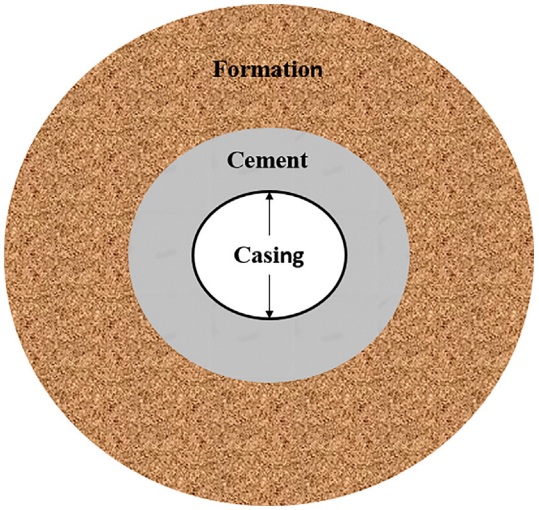

Fig. 20. Compressive strength of specimens.

3.6. Conclusion

The article presents the results of ANF reinforced cementitious composites at different concentrations of ANFs (0, 0.1, 0.2, and 0.3 wt%) subjected to various simulated wellbore testing and microstructural analysis. The conclusions of these investigations are summarized as follows:

(1) Proper dispersion of nanofilaments is a requirement when the intent is to enhance mechanical properties and improve microstructural behavior. According to the TEM images, the pre-dispersed solution had a better dispersion than the ball milled solution due to varying dispersive methodologies.
(2) All cement composite formulations were able to withstand confining pressure cycling considering there was no dramatic increase in permeability. Although, the ANF-1 formulation possessed the lowest permeability at 1.44 μD. This is

essentially due to the high aqueous adsorption capacity to water, allowing the formation of C-S-H around ANF's creating a denser microstructure with lower permeability than the Ref sample. The permeability, however, gradually increases with higher dosages of ANF's causing the formation of nano and microcracks due to irregularities in the pore structures.

(3) The compressive strength was the highest for the ANF-1 formulation at 25.6 MPa compared to Ref. at 17.8 MPa. This is largely due to the "bridging effect" of nanofilaments and the increase in C-S-H. However, at higher dosage of ANF's, the compressive strength decreases due to nanofiber clustering.

(4) All cement formulations experienced low inelastic deformation during confining pressure cycling. ANF-1 possessed the lowest MOE among all the formulations and the lowest discrepancy between the V_p and V_s waves during pressure cycling. This is further indication that the ANF-1 formulation contained the least amount of pore spaces after hydration. ANF-1 also possesses the highest Poisson's ratio among all cement formulations. The low MOE and high Poisson's Ratio essentially indicated better ductility and thus a higher probability of resisting deformation due to casing expansion/contraction.

(5) All cement formulation experienced the same XRD pattern with only variations in the diffraction peaks. ANF-1 possessed the highest amount of C-S-H due primarily to the nucleation effect (seeding effect) which provides additional surface area for nucleation sites of C-S-H formation.

(6) The DOH was the highest for the ANF-1 formulation due to the seeding effect, which effectively enhances hydration. This increase in hydration essentially improves the mechanical performance and microstructural properties of the cement composites.

(7) ANF is a relatively inexpensive material, with substantial potential to be utilized in the oil well cement industry. Essentially, ANF can help to avoid secondary cement jobs and improve the overall wellbore integrity.

CRediT authorship contribution statement

P.D. McElroy: Investigation. **H. Emadi:** Supervision. **D. Unruh:** Formal analysis.

Declaration of Competing Interest

The authors declare that they have no known competing financial interests or personal relationships that could have appeared to influence the work reported in this paper.

Acknowledgments

The authors would like to thank Halliburton for providing the cement and additives to complete this project. The authors would also like to acknowledge the Maddox Engineering Research Center at Texas Tech University for allowing the usage of the TGA equipment and the Experimental Science Building at Texas Tech University for assisting in conducting the (TEM) analysis.

References

[1] W.C. Jimenez, J.A. Urdaneta, X. Pang, J.R. Garzon, G. Nucci, H. Arias, Innovation of annular sealants during the past decades and their direct relationship with on/offshore wellbore economics, Soc. Petrol. Eng. (2016), https://doi.org/10.2118/180041-MS.

[2] T. Vrålstad, R. Skorpa, B. Werner, Experimental Studies on cement sheath integrity during pressure cycling, Soc. Petrol. Eng. (2019), https://doi.org/10.2118/194171-MS.

[3] Fei Yin, D. Hou, W. Liu, Y. Deng, Novel assessment and countermeasure for micro-annulus initiation of cement sheath during injection/fracturing, Fuel 252 (2019) (2019) 157–163, https://doi.org/10.1016/j.fuel.2019.04.018.

[4] Richard J. Davies, S. Almond, R.S. Ward, R.B. Jackson, C. Adams, F. Worrall, L.G. Herringshaw, J.G. Gluyas, M.A. Whitehead, Oil and gas wells and their integrity: implications for shale and unconventional resource exploitation, Marine Petrol. Geol. 59 (2015) (2014) 674–675, https://doi.org/10.1016/j.marpetgeo.2014.07.014.

[5] Xiuxuan Sun, Q. Wu, S. Lee, Y. Qing, Y. Wu, Cellulose nanofibers as a modifier for rheology, curing and mechanical performance of oil well cement, Sci. Rep. 6 (1) (2016) 2016, https://doi.org/10.1038/srep31654.

[6] Narjes Jafariesfad, M.R. Geiker, Y. Gong, P. Skalle, Z. Zhang, J. He, Cement sheath modification using nanomaterials for long-term zonal isolation of oil wells: review, J. Petrol. Sci. Eng. 156 (2017) (2017) 662–672, https://doi.org/10.1016/j.petrol.2017.06.047.

[7] Z.S. Metaxa, M.S. Konsta-Gdoutos, S.P. Shah, Mechanical properties and nanostructure of cement-based materials reinforced with carbon nanofibers and Polyvinyl Alcohol (PVA) microfibers ACI Spec. Publ. 270 SP, American Concrete Institute, 2010, pp. 115–126.

[8] Florence Sanchez, Konstantin Sobolev, Nanotechnology in concrete–a review, Constr. Build. Mater. 24 (11) (2010) 2060–2071.

[9] A. Vijayabhaskar, M. Shanmugasundaram, Usage of carbon nanotubes and nano fibers in cement and concrete: a review, Int. J. Eng. Technol. 9 (2) (2017) 564–569, https://doi.org/10.21817/ijet/2017/v9i2/170902045.

[10] S. Ahmed, C.P. Ezeakacha, S. Salehi, Improvement in cement sealing properties and integrity using conductive carbon nano materials: from strength to thickening time, Soc. Petrol. Eng. (2018), https://doi.org/10.2118/191709-MS.

[11] M.K. Rahman, W.A. Khan, M.A. Mahmoud, P. Sarmah, MWCNT for enhancing mechanical and thixotropic properties of cement for HPHT applications, Offshore Technol. Conf. (2016), https://doi.org/10.4043/26465-MS.

[12] Mohammed Mousa M. Alkhamis, New wellbore-integrity classification for gas migration problems and new cement formulations using Graphene Nano Platelets to prevent gas migration through cement (2018). Masters Theses 7751. http://scholarsmine.mst.edu/masters_theses/7751.

[13] Tanvir Manzur, Nur Yazdani, Effect of different parameters on properties of multiwalled carbon nanotube-reinforced cement composites, Arabian J. Sci. Eng. 41 (12) (2016) 4835–4845, https://doi.org/10.1007/s13369-016-2181-8.

[14] K.M. Liew, M.F. Kai, L.W. Zhang, Mechanical and damping properties of CNT-reinforced cementitious composites, Compos. Struct. 160 (2017) (2016) 81–88, https://doi.org/10.1016/j.compstruct.2016.10.043.

[15] Valentin S. Romanov, S.V. Lomov, I. Verpoest, L. Gorbatikh, Stress magnification due to carbon nanotube agglomeration in composites, Compos. Struct. 133 (2015) (2015) 246–256, https://doi.org/10.1016/j.compstruct.2015.07.069.

[16] B. Iverson, R. Darbe, D. McMechan, Evaluation of Mechanical Properties of Cements, American Rock Mechanics Association, 2008.

[17] K.J. Goodwin, R.J. Crook, Cement sheath stress failure, SPE Drilling Eng. 7 (04) (1992) 291–296, https://doi.org/10.2118/20453-pa.

[18] Zhaoguang Yuan, The Effect of Cement Mechanical Properties and Reservoir Compaction on HPHT Well Integrity" Doctoral dissertation, A&M University, Texas, 2012.

[19] Kris Ravi, D.E. McMechan, B.R. Reddy, R. Crook, A comparative study of mechanical properties of density-reduced cement compositions, SPE Annual Technical Conference and Exhibition, 2004, doi:10.2118/90068-ms.

[20] M.R. Dousti, Y. Boluk, V. Bindiganavile, The effect of cellulose nanocrystal (CNC) particles on the porosity and strength development in oil well cement paste, Constr. Build. Mater. 205 (2019) 456–462, https://doi.org/10.1016/j.conbuildmat.2019.01.073.

[21] M. Aghayan, I. Hussainova, M. Gasik, M. Kutuzov, M. Friman, Coupled thermal analysis of novel alumina nanofibers with ultrahigh aspect ratio, Thermochim. Acta 574 (2013) 140–144, https://doi.org/10.1016/j.tca.2013.10.010.

[22] Tengfei Fu, R.J. Moon, P. Zavattieri, J. Youngblood, W.J. Weiss, Cellulose nanomaterials as additives for cementitious materials, Cellulose-Reinforced Nanofibre Compos. (2017) 455–482, https://doi.org/10.1016/b978-0-08-100957-4.00020-6.

[23] Alexandre Lavrov, Malin Torsaeter, Physics and Mechanics of Primary Well Cementing, Springer, Berlin Heidelberg, 2016.

[24] D. Guner, H. Ozturk, Comparison of mechanical behaviour of G class cements for different curing time, 24th International Mining Congress and Exhibition Turkey, 2015.

[25] Eric Broni-Bediako, O.F. Joel, G. Ofori-Sarpong, Oil well cement additives: a review of the common types, Oil Gas Res. 02 (02) (2016), https://doi.org/10.4172/2472-0518.1000112.

[26] Abdullah Saleh Al-Yami, J. Ramasamy, V. Wagle, Chemical additives for oil well cementing, Res. Rev. J. Chem. (2017).

[27] Seeyed Arash Ahmadi, J.T. Shakib, A. Ghaderi, A. Beirami, The performance of foam cement in Iran oil wells and comparison of bentonite light cement with foam cement and presentation of foam cement advantages in Iran oil wells, Aust. J. Basic Appl. Sci. (2013) 696–702.

[28] American Petroleum Institute, 2013. Recommended Practice for Testing Well Cements. API. Specification 10B-2 Second Edition.

[29] E.B. Nelson, D. Guillot, Well Cementing, Schlumberger, Sugar Land, TX, 2006.

[30] J.C. Le-Minous, D. Mutti, A. Bouvet, I. Unanue-Rodriguez, A. Chang, I. Massie, E. Schnell, Permeability study of API class G and B cements considering seawater and WBM contamination, Soc. Petrol. Eng. (2017), https://doi.org/10.2118/184613-MS.
[31] Jose M. Carcione, Fabio Cavallini, Poisson's ratio at high pore pressure, Geophys. Prospect. 50 (1) (2002) 97–106, https://doi.org/10.1046/j.1365-2478.2002.00299.x.
[32] NER, Autolab 1500 Operations Manual, New England Research Inc., Vermont, USA, 2014.
[33] W.F. Brace, J.B. Walsh, W.T. Frangos, Permeability of granite under high pressure, J. Geophys. Res. 73 (1968) 2225–2236.
[34] J.D. Bredehoeft, I.S. Papadopoulas, A method for determining the hydraulic properties of tight formations, Water Resour. Res. 15 (1980) 233–238.
[35] B. Evans, T.F. Wong, Fault Mechanics and Transport Properties of Rocks, Academic Press, New York, 1992.
[36] D.M. Roy, B.E. Scheetz, J. Pommersheim, P.H. Licasttro, Development of Transient Permeability Theory and Apparatus for Measurements of Cementitious Materials, Strategic Highway Research Program, Washington, D.C., 1993.
[37] D.T. Mueller, V. GoBoncan, R.L. Dillenbeck, T. Heinold, Characterizing casing-cement-formation interactions under stress conditions: impact on long-term zonal isolation, Soc. Petrol. Eng. (2004), https://doi.org/10.2118/90450-MS.
[38] Riichi Murayama, M. Kobayashi, C. Jen, Study of material evaluation probe using a longitudinal wave and a transverse wave, J. Sensor Technol. 03 (02) (2013) 25–29, https://doi.org/10.4236/jst.2013.32005.
[39] Joana Roncero, S. Valls, R. Gettu, Study of the influence of superplasticizers on the hydration of cement paste using nuclear magnetic resonance and X-ray diffraction techniques, Cem. Concr. Res. 32 (1) (2002) 103–108, https://doi.org/10.1016/s0008-8846(01)00636-6.
[40] N.B. Singh, Sarita Rai, Effect of polyvinyl alcohol on the hydration of cement with rice husk ash, Cem. Concr. Res. 31 (2) (2001) 239–243, https://doi.org/10.1016/s0008-8846(00)00475-0.
[41] Axel Schöler, B. Lothenbach, F. Winnefeld, M. Zajac, Hydration of quaternary portland cement blends containing blast-furnace slag, siliceous fly ash and limestone powder, Cem. Concr. Compos. (55, 2015,) 374–382, https://doi.org/10.1016/j.cemconcomp.2014.10.001.
[42] Yeonung Jeong, C.W. Hargis, S. Chun, J. Moon, Effect of calcium carbonate fineness on calcium sulfoaluminate-belite cement, Materials 10 (8) (2017) 900, https://doi.org/10.3390/ma10080900.
[43] Ivindra Pane, Will Hansen, Investigation of blended cement hydration by isothermal calorimetry and thermal analysis, Cem. Concr. Res. 35 (6) (2005) 1155–1164, https://doi.org/10.1016/j.cemconres.2004.10.027.
[44] Yanlei Wang, Y. Wang, B. Wan, B. Han, G. Cai, Z. Li, Properties and mechanisms of self-sensing carbon nanofibers/epoxy composites for structural health monitoring, Compos. Struct. (200, 2018,) 669–678, https://doi.org/10.1016/j.compstruct.2018.05.151.
[45] A. Yazdanbaksh, Zachary Grasley, B. Tyson, Rashid Abu Al-Rub, Carbon nanofibers and nanotubes in cementitious materials: some issues on dispersion and interfacial bond, ACI SP. 267, 2009, 21–34.
[46] Yonathan Reches, K. Thomson, M. Helbing, D.S. Kosson, F. Sanchez, Agglomeration and reactivity of nanoparticles of SiO_2, TiO_2, Al_2O_3, Fe_2O_3, and clays in cement pastes and effects on compressive strength at ambient and elevated temperatures, Constr. Build. Mater. 167 (2018) 860–873, https://doi.org/10.1016/j.conbuildmat.2018.02.032.
[47] G. Gkikas, N.-M. Barkoula, A.S. Paipetis, Effect of dispersion conditions on the thermo-mechanical and toughness properties of multi walled carbon nanotubes-reinforced epoxy, Compos. B Eng. 43 (6) (2012) 2697–2705, https://doi.org/10.1016/j.compositesb.2012.01.070.
[48] Ahmed Abdulhamid Mahmoud, S. Elkatatny, A. Ahmed, R. Gajbhiye, Influence of nanoclay content on cement matrix for oil wells subjected to cyclic steam injection, Materials 12 (9) (2019) 1452, https://doi.org/10.3390/ma12091452.
[49] Scott W. Muzenski, The Design of High Performance and Ultra-High Performance Fiber Reinforced Cementitious Composites with Nano Materials" (2015).Theses and Dissertations. Paper 902.
[50] M.R. Noordin, K.Y. Liew, Synthesis of alumina nanofibers and composites, Nanofibers (2010), https://doi.org/10.5772/8165.
[51] R. Spaulding, I. Haljasmaa, J. Fazio, C. Gieger, B. Kutchko, J. Gardiner, et al., An assessment of the dynamic moduli of atmospherically generated foam cements, Offshore Technol. Conf. (2015), https://doi.org/10.4043/25776-MS.
[52] K. Kopp, S. Reed, J. Foreman, B. Carty, J. Griffith, Foamed cement vs. conventional cement for zonal isolation-case histories, Soc. Petrol. Eng. (2000), https://doi.org/10.2118/62895-MS.
[53] S. Muzenski, I. Flores-Vivian, K. Sobolev, Ultra-high strength cement-based composites designed with aluminum oxide nano-fibers, Constr. Build. Mater. 220 (2019) 177–186, https://doi.org/10.1016/j.conbuildmat.2019.05.175.
[54] Nicola Meller, K. Kyritsis, C. Hall, The Mineralogy of the $CaO–Al_2O_3–SiO_2–H_2O$ (CASH) Hydroceramic System from 200 to 350 °C, Cem. Concr. Res. 39 (1) (2009) 45–53, https://doi.org/10.1016/j.cemconres.2008.10.002.
[55] J.F. Young, W. Hansen, Volume relationships for C–S–H formation based on hydration stoichiometry, in: L. Struble, P. Brown, (Eds.,), MRS proceedings, 1986, pp. 313–820.
[56] J. Zhang, E.A. Weissinger, S. Peethamparan, G.W. Scherer, Early hydration and setting of oil well cement, Cem. Concr. Res. 40 (7) (2010) 1023–1033, https://doi.org/10.1016/j.cemconres.2010.03.014.
[57] P. Mounanga, A. Khelidj, A. Loukili, V. Baroghel-Bouny, Predicting Ca(OH)2 content and chemical shrinkage of hydrating cement pastes using analytical approach, Cem. Concr. Res. 34 (2) (2004) 255–265, https://doi.org/10.1016/j.cemconres.2003.07.006.